Chapter 5:

Facile Synthesis and Characterization of Strontium Sulfide Incorporated Graphitic Carbon Nitride Nanocomposite for Energy Storage Applications

Muhammad Arshad Kamran, Wajeeha Sameen, Areej Rani

DOI: 10.21467/books.186.5
Additional information is available at the end of the chapter

Strontium sulfide/graphitic carbon nitride (SrS/g-C_3N_4) nanocomposites were successfully synthesized via a facile hydrothermal method to improve the optical and electrochemical performance of SrS for energy storage and optoelectronic applications. The synthesized nanohybrids were systematically characterized using X-ray diffraction (XRD), UV–Vis spectroscopy, photoluminescence (PL), Raman spectroscopy, and electrochemical techniques. XRD analysis confirmed the successful formation of the composite and revealed enhanced crystallinity with increasing g-C_3N_4 content. UV–Vis results demonstrated a reduced optical band gap, indicating improved visible-light absorption after g-C_3N_4 incorporation. PL spectra exhibited a characteristic emission peak at 445 nm with suppressed charge carrier recombination, while Raman analysis verified the successful integration of g-C_3N_4 into the SrS matrix. Electrochemical investigations demonstrated that the optimized 0.3% SrS/g-C_3N_4 nanohybrid delivered a high specific capacitance of 850 F g^{-1} at a current density of 2 A g^{-1}, together with an energy density of 38.19 Wh kg^{-1} and a power density of 500 W kg^{-1}. The enhanced performance is attributed to the synergistic interaction between SrS and g-C_3N_4, which facilitates charge transport and increases electroactive sites. These results demonstrate that SrS/g-C_3N_4 nanohybrids are promising multifunctional materials for advanced high-performance supercapacitor applications as well as optoelectronic devices.

1. Introduction

The increasing global demand for energy, coupled with the depletion of fossil fuel resources and growing environmental concerns, has intensified the search for sustainable and efficient energy storage technologies. Among various energy storage systems, electrochemical energy storage devices, particularly supercapacitors (SCs), have attracted significant attention owing to their high-power density, rapid charge–discharge capability, long cycling stability, and environmental friendliness. However, the practical application of SCs is still limited by the relatively low energy density of conventional electrode materials. Consequently, considerable research efforts have been devoted to the development of advanced nanostructured electrode materials with high electrical conductivity, large specific surface area, abundant electrochemically active sites, and fast ion diffusion kinetics [1-4].

Nanostructured composite materials have attracted considerable attention because they combine the beneficial characteristics of two or more individual components, resulting in enhanced physicochemical properties that cannot be achieved by single-phase materials. Owing to their large specific surface area,

ISBN: 978-81-998984-9-3

tunable electronic structure, improved charge transport, and abundant active sites, nanocomposites have demonstrated remarkable potential in photocatalysis, optoelectronics, supercapacitors, sensors, and renewable energy technologies. The synergistic interaction between constituent materials often improves light harvesting, suppresses charge carrier recombination, and facilitates rapid electron transport, thereby significantly enhancing device performance [5-10].

Among emerging semiconductor materials, graphitic carbon nitride (g-C_3N_4) has received significant attention because of its unique electronic structure, metal-free composition, excellent thermal and chemical stability, low cost, and facile synthesis from nitrogen-rich precursors. With a moderate band gap of approximately 2.7 eV, g-C_3N_4 can absorb visible light and has been extensively investigated for photocatalysis, hydrogen evolution, environmental remediation, photoelectrochemical devices, and optoelectronics. Furthermore, its band structure can be tailored through morphological engineering, elemental doping, and heterojunction formation, making it a versatile platform for multifunctional applications [11-16]. Recent studies have demonstrated that g-C_3N_4-based semiconductor heterostructures exhibit significantly enhanced optical and electrochemical properties due to improved charge separation and extended visible-light absorption. Xiu-Li Luo et al. synthesized g-C_3N_4/NiS/$SrTiO_3$ nanocomposites via a hydrothermal method and reported enhanced photocatalytic performance resulting from efficient interfacial charge transfer and suppressed electron–hole recombination g-C_3N_4/NiS/$SrTiO_3$ [17].

Similarly, Wang *et al.* prepared g-C_3N_4/ZnS composites through chemical precipitation and demonstrated improved visible-light absorption and structural stability, highlighting their potential for optoelectronic applications [18]. Vignesh *et al.* fabricated ZnO–Ag_2O/g-C_3N_4 heterostructures with excellent photocatalytic activity and stability owing to effective heterojunction formation [19]. Vinoth *et al.* reported that CSO-g-C_3N_4 nanohybrids exhibited enhanced optical and electrochemical properties, making them promising materials for energy storage and conversion applications [20]. Likewise, Paul *et al.* showed that ZnO/g-C_3N_4 composites possess enhanced visible-light absorption and improved charge carrier separation, leading to superior photoactivity [21]. Jiang *et al.* further demonstrated that g-C_3N_4/CdS heterojunctions broaden the visible-light response and improve solar energy conversion efficiency [22]. A comprehensive review by Safaei *et al.* highlighted the growing potential of g-C_3N_4-based materials for solar cells, electrocatalysis, SCs, and other advanced energy-related applications while emphasizing the need for developing new g-C_3N_4- based heterostructures with improved multifunctional performance [23].

Despite all the advantages, pristine g-C_3N_4 still suffers from several intrinsic limitations that restrict its practical performance. These include limited visible-light absorption, poor electrical conductivity, low charge carrier mobility, and rapid recombination of photogenerated electron–hole pairs. Such shortcomings significantly reduce its efficiency in and electrochemical energy storage and optoelectronic applications. Various strategies, including elemental doping, defect engineering, heterostructure construction, and composite formation, have therefore been explored to overcome these limitations. Among these approaches, constructing semiconductor heterojunctions has proven particularly effective because it

promotes efficient charge separation, extends light absorption, and enhances interfacial charge transfer [24-26].

Strontium sulfide (SrS), an alkaline-earth metal sulfide, is another promising wide-bandgap semiconductor with excellent optical transparency, chemical stability, and favorable electronic properties. SrS crystallizes in a stable rock-salt structure and possesses a band gap ranging from approximately 3.8 to 4.2 eV, making it suitable for phosphors, luminescent devices, optical coatings, radiation detectors, sensors, and other optoelectronic applications. The material also exhibits good thermal stability and environmental durability, making it an attractive candidate for developing advanced semiconductor composites. However, its relatively wide band gap limits visible-light absorption, which restricts its standalone performance in practical optoelectronic devices [27, 28].

Combining SrS with g-C_3N_4 provides an effective strategy for overcoming the limitations of both materials. The formation of a SrS/g-C_3N_4 heterostructure is expected to facilitate efficient charge separation at the interface, improve electrical conductivity, suppress electron–hole recombination, and increase the availability of electrochemically active sites. In addition, the intimate interfacial contact between the two semiconductors can broaden optical absorption and accelerate charge transfer kinetics, leading to enhanced optical and electrochemical performance. Such synergistic interactions make SrS/g-C_3N_4 nanohybrids attractive candidates for multifunctional applications including optoelectronics, photocatalysis, sensing, and energy storage. These composites can enhance light absorption, improve by increasing the catalyst's surface area, and improve electron transfer rates by creating additional pathways for electron transport [29, 30].

Although considerable research has been devoted to g-C_3N_4- based composites, studies involving SrS/ g-C_3N_4 nanohybrids remain scarce, particularly regarding their electrochemical energy storage behavior. Most previous investigations have primarily focused on photocatalytic applications, while the electrochemical characteristics of SrS/g-C_3N_4 composites have received limited attention. Moreover, the development of a simple, cost-effective, and scalable synthesis approach capable of producing homogeneous SrS/g C_3N_4 nanohybrids with controlled composition and enhanced multifunctional properties remains an important challenge.

In the present work, SrS/g-C_3N_4 nanohybrids were successfully synthesized using a facile hydrothermal method with varying g-C_3N_4 concentrations. The structural, optical, and electrochemical properties of the synthesized nanohybrids were systematically investigated using X-ray diffraction (XRD), UV–Visible spectroscopy, Raman spectroscopy, photoluminescence (PL), and electrochemical techniques. The influence of g-C_3N_4 incorporation on crystallinity, optical band gap, charge carrier dynamics, and charge storage performance was comprehensively evaluated. The optimized SrS/g-C_3N_4 nanohybrid exhibited significantly improved electrochemical performance, demonstrating its potential as a multifunctional material for next-generation and high-performance energy storage systems and optoelectronic devices.

2. Experimental

2.1. Materials

Melamin ($C_3H_6N_6$), Graphitic carbon nitride (g-C_3N_4), Strontium nitrate [$Sr(NO_3)_2.6H_2O$], Sodium sulfide (Na_2S), Strontium sulfide (SrS), Ethanol (C_2H_5OH) are bought from Sigma-Aldrich. Nickel foam (substrate) is acquired from MTI USA. All of the chemicals were purchased at analytical grade, and they were utilized without additional purification. Moreover, deionized water was used during the whole experimentation.

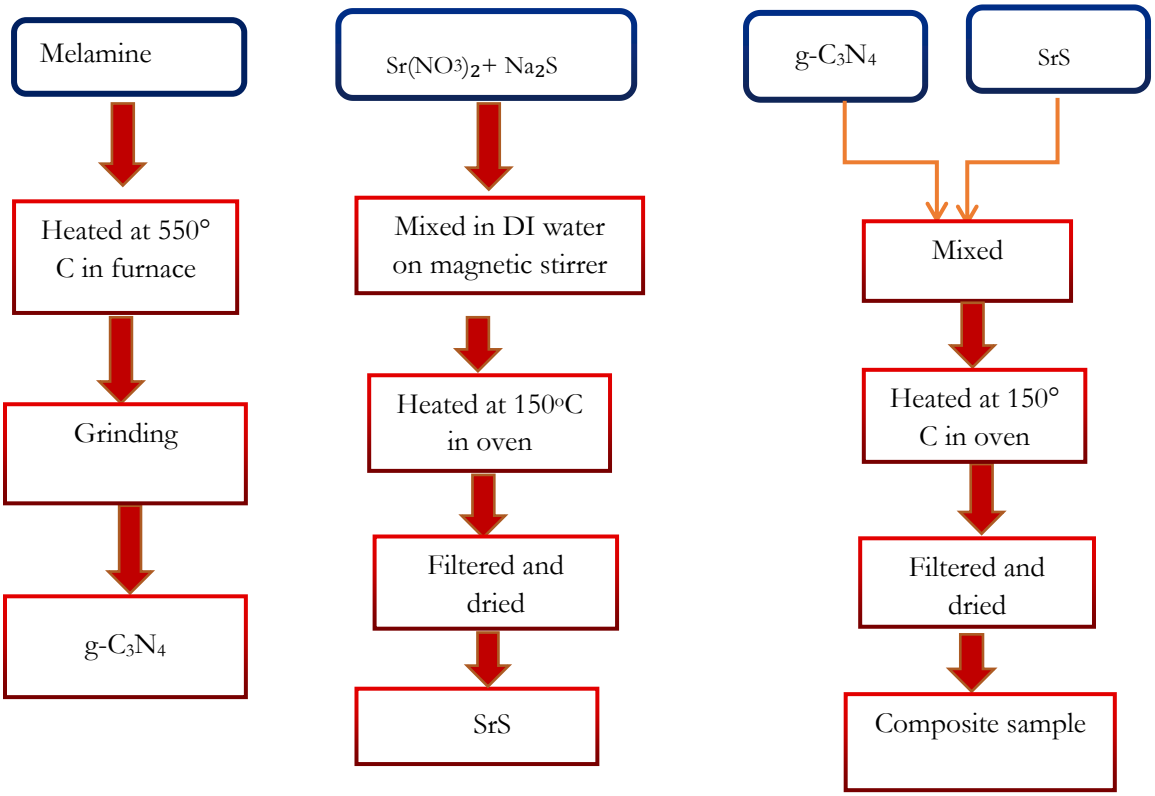

Figure 5.1 Schematic diagram of the synthesis method.

2.2. Fabrication of graphitic carbon nitride (g-C_3N_4)

Graphitic carbon nitride (g-C_3N_4) was synthesized using a conventional thermal polymerization method. Briefly, 20 g of melamine ($C_3H_6N_6$) was weighed and placed in an alumina crucible with a tightly fitted lid. The crucible was then transferred to a muffle furnace and heated gradually from room temperature to 550 °C at a controlled heating rate. The temperature was maintained at 550 °C for 4 h to ensure complete polymerization of the precursor. After naturally cooling to room temperature, a yellow-colored g-C_3N_4 product was obtained, as shown in **Figure 5.1**. The as-prepared material was ground into a fine powder using an agate mortar and pestle and stored for subsequent synthesis and characterization.

2.3. Synthesis of SrS Nanostructures

SrS was synthesized via a hydrothermal method. Briefly, 0.529 g of $Sr(NO_3)_2 \cdot 6H_2O$ was dissolved in 25 mL of deionized water and stirred for 30 min. Separately, 0.275 g of Na_2S was dissolved in 25 mL of deionized water and added dropwise to the $Sr(NO_3)_2$ solution under continuous stirring. The reaction mixture was

further stirred for 10 min, transferred into a Teflon-lined stainless-steel autoclave, and heated at 150 °C for 4 h. After naturally cooling to room temperature, the obtained precipitate was filtered, washed several times with deionized water and ethanol, and dried to obtain pure SrS powder.

2.4. Synthesis of SrS/g-C_3N_4 Nanocomposite

SrS/g-C_3N_4 nanocomposites were synthesized by incorporating 0.1, 0.2, 0.3, and 0.4 g of graphitic carbon nitride (g-C_3N_4) into the previously synthesized SrS using the same synthesis procedure described above. Pure SrS and g-C_3N_4 were also prepared separately for comparison. The obtained nanocomposites were subsequently characterized to investigate the effect of g-C_3N_4 incorporation on their structural, optical, and electrochemical properties. A schematic diagram of the sample preparation is shown in the **Figure 5.1**.

2.5. Characterization Techniques

The crystalline structures of the synthesized materials (g-C_3N_4, SrS, and Srs/gC_3N_4 NCs) were characterized by JDX-3532 diffractometer made by JEOL, Japan with Cu Kα radiation of wavelength (1.5418Å) operated at 2θ range from 10° to 70°. The morphology of the fabricated electrode materials was explored using MIRA3 TESCAN SEM running at a 5.0 KV accelerating voltage. Elemental analyses of the samples were carried out through EDX incorporated with the SEM. The photoluminescence (PL) spectra were taken via Edinburgh Instruments FLS920 spectrofluorometer. The UV-Vis absorbance studies of the samples were recorded by Peak Instrument (Model C7200) in the range of 190–700 nm. Fourier-transform infrared spectroscopy (FTIR) analysis was executed to confirm the molecular configuration of the materials in the range of 400–4000 cm^{-1}.

2.6. Electrochemical measurements

All the electrochemical studies of the designed electrodes were evaluated via an electrochemical workstation GAMRY Reference 3000 (42012). The working electrode was designed by mixing 10 wt. % activated carbon, 5 wt. % nafion, and 85 wt. % of the active material. Attained slurry was pressed on a piece of Ni foam (2.5×1.5 cm^2) which was then dried at 70^o C for 8 hours. The mass loading of the synthesized electrode was ~2 mg. In a three-electrode system, a platinum wire functioned as the counter electrode, an Ag/AgCl electrode acted as the reference electrode, and a 2 M KOH aqueous solution served as the electrolyte. The electrochemical performance of designed electrodes was evaluated via cyclic voltammetry (CV), constant-current galvanostatic-charge-discharge (GCD), and electrochemical impedance spectroscopy (EIS).

3. Results and Discussion

3.1. Scanning Electron Microscope (SEM)

The morphology of the as-synthesized materials (g-C_3N_4, SrS, and Srs/gC_3N_4 NCs) was studied by SEM at different magnificenceScanning electron microscopy (SEM) was used to study the surface morphology of the synthesized g-C_3N_4, SrS, and Srs/gC_3N_4 NCs (depicted in **Figure. 5.2**). SEM images of pure g-C_3N_4

(Figure 5.2(a_1-b_1)) show a flake-like morphology with randomly stacked and interconnected nanosheets, resulting in a high surface area for interfacial interactions. In contrast, pure SrS (as displayed in **Figure 5.2(a_1-b_1))** has a well-defined nanorod-like morphology, with rod-shaped crystallites equally distributed and collected into clusters. The development of these nanorods is due to anisotropic crystal growth during the hydrothermal synthesis process.

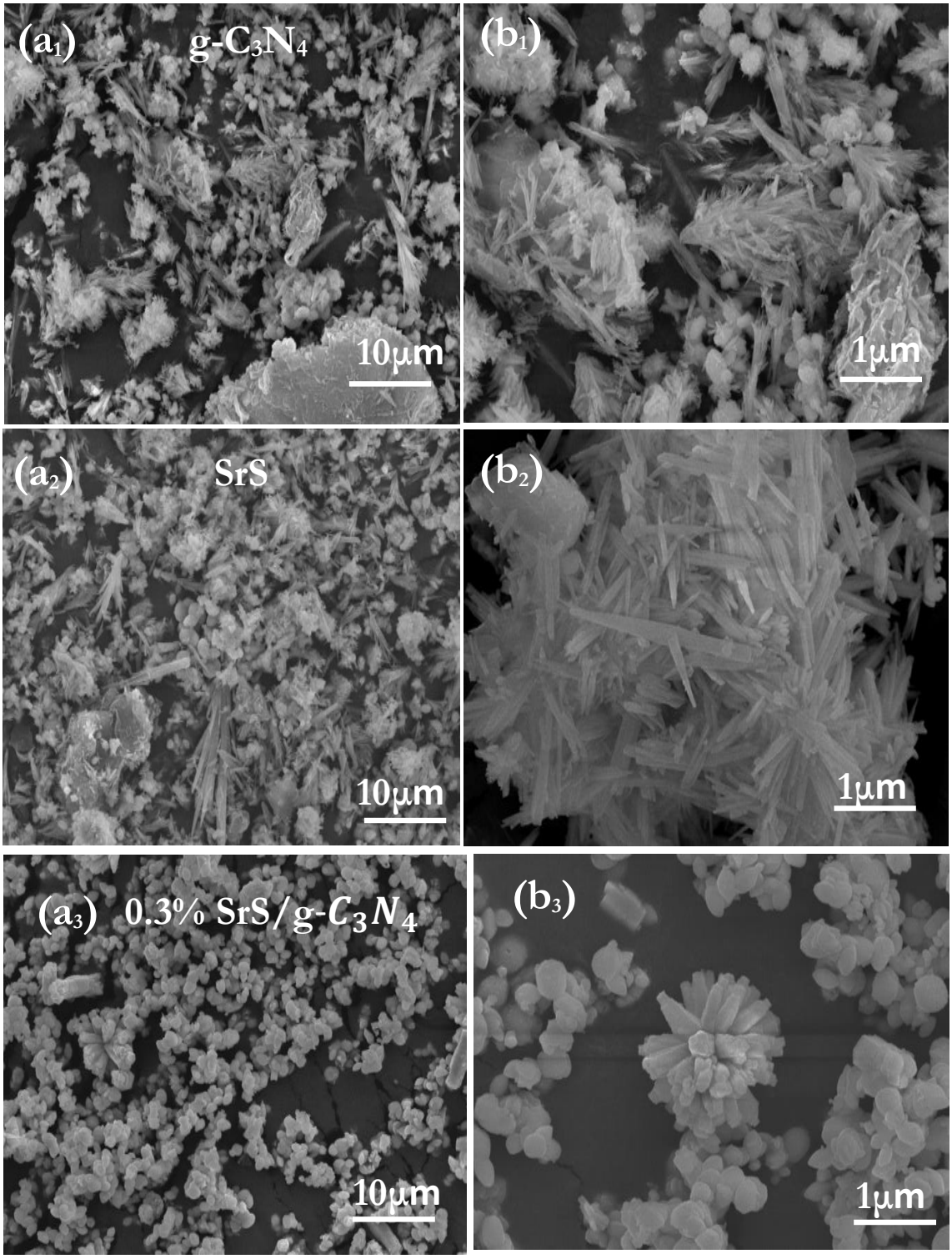

Figure 5.2. SEM Micrographs of (a_1,b_1) gC_3N_4 NSs, (a_2,b_2) SrS NSs (a_3,b_3)0.3 SrS/gC_3N_4 NCs

After incorporating gC_3N_4 into the SrS matrix, the optimized 0.3 SrS/g-C_3N_4 NC (**Figure 5.2(a_3-b_3)**) displays a flower-like hierarchical architecture, formed by the uniform assembly of SrS nanorods over the gC_3N_4 sheets. This unique morphology provides a porous and interconnected network with abundant electrochemically active sites and enlarged electrode/electrolyte contact area. Such a hierarchical structure

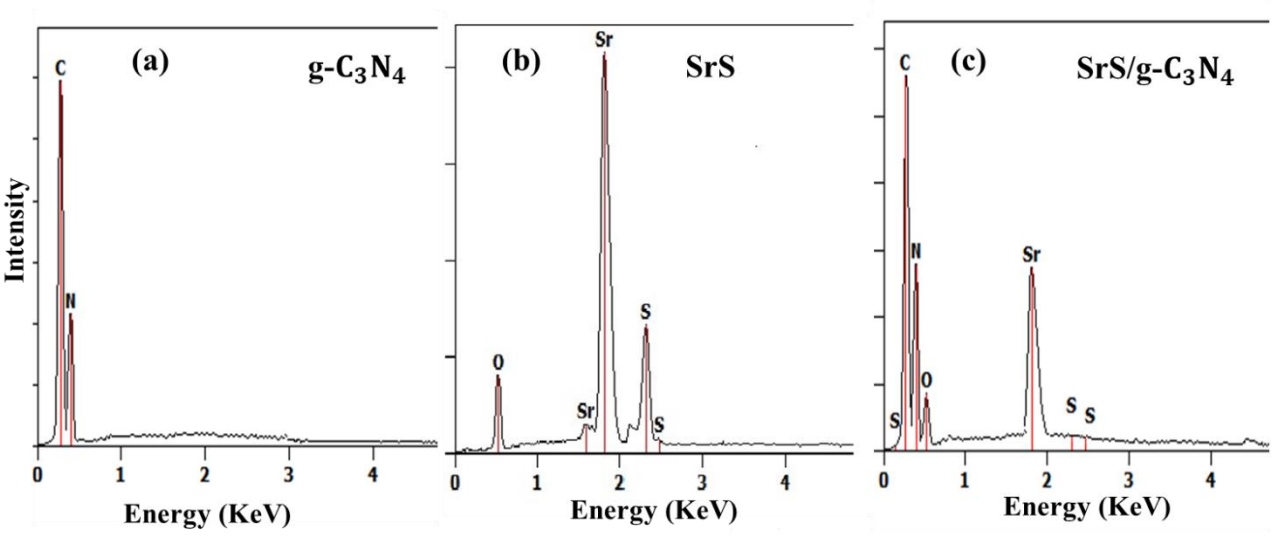

Figure 5.3 EDX spectra of a) g-C_3N_4 NSs, b) SrS NSs, and c) 0.3% SrS/g-C_3N_4 NCs.

is expected to facilitate rapid ion diffusion and electron transport while suppressing particle agglomeration. The improved structural characteristics are therefore beneficial for enhancing the electrochemical charge storage behavior and are anticipated to contribute to the superior specific capacitance of the SrS/ gC_3N_4 NC.

3.2. Energy Dispersive X-ray (EDX) Spectroscopy

The elemental composition and chemical purity of the synthesized materials were investigated using energy-dispersive X-ray spectroscopy (EDX), with the resulting spectra shown in **Figure 5.3**. The EDX spectrum of pure g-C_3N_4 (as depicted in **Figure 5.3(a))** shows characteristic peaks belonging entirely to carbon (C) and nitrogen (N), demonstrating the successful synthesis of g-C_3N_4 with no detectable impurities. The EDX spectrum of pure SrS (as displayed **Figure 5.3(b))** shows strong peaks of strontium (Sr) and sulphur (S), demonstrating the effective synthesis of SrS. A faint oxygen (O) signal is also found, which could be caused by minor surface oxidation or adsorbed oxygen species during sample handling.

The EDX spectrum of the 0.3 SrS/g-C_3N_4 NC (as depicted in **Figure 5.3(c)**) shows the typical peaks of C, N, Sr, and S, demonstrating the effective incorporation of SrS into the g-C_3N_4 matrix. There are no further impurity peaks found, indicating that the nanocomposite was synthesised with high purity. The presence of all constituent materials confirms the successful development of the SrS/g-C_3N_4 heterostructure.

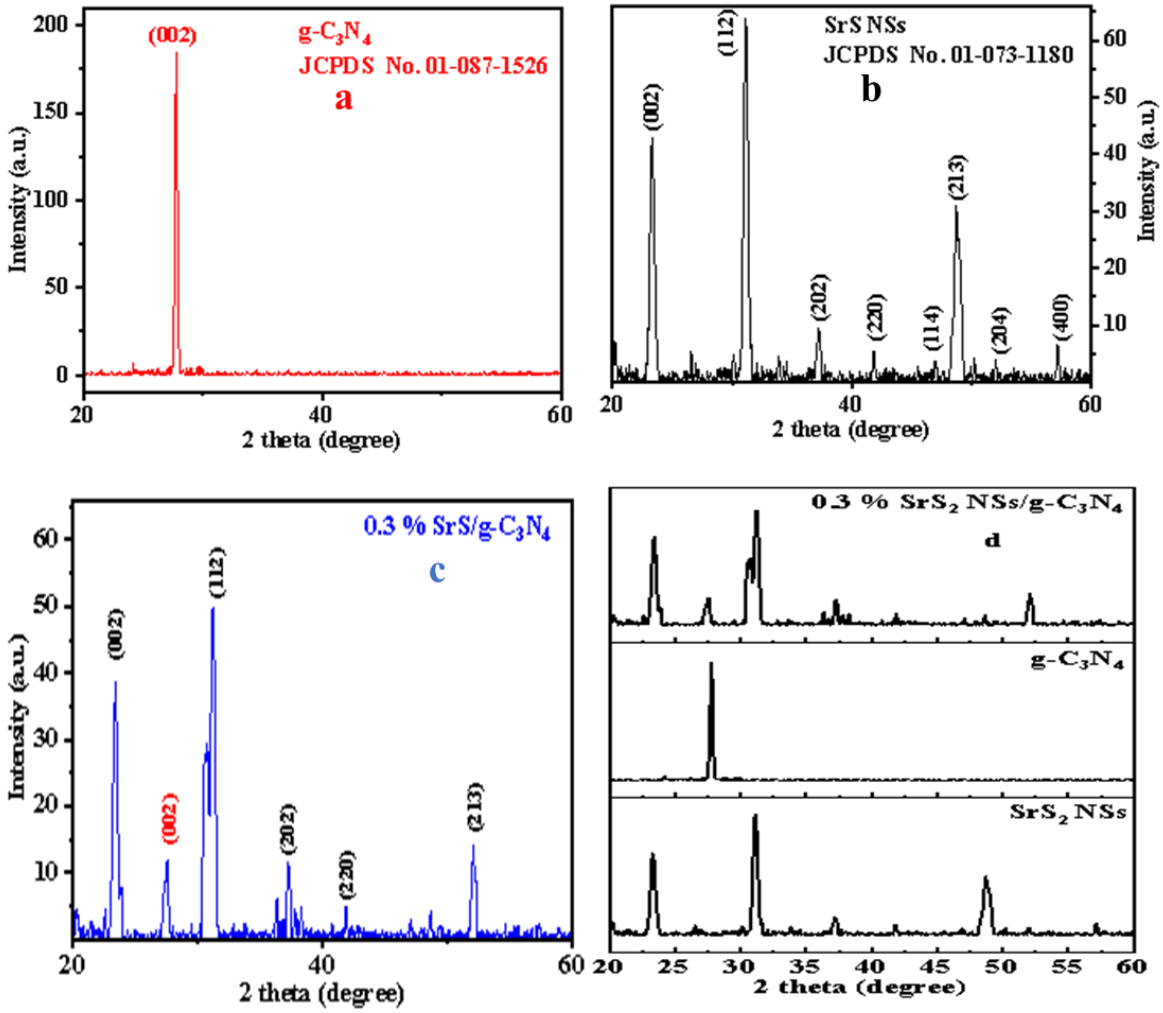

Figure 5.4 XRD pattern of **(a)** g-C_3N_4 **(b)** SrS_2 NSs **(c)** 0.3% SrS_2/g-C_3N_4 **(d)** XRD stack plot at an angle of 27.8°.

3.3. X-Ray Diffraction (XRD)

The crystal structure and phase purity of pristine g-C_3N_4, SrS**,** and the 0.3% SrS/g-C_3N_4 NC were examined by X-ray diffraction (XRD), as shown in **Figure 5.4**. The XRD pattern of pristine g-C_3N_4. (**Figure 5.4(a**) exhibits a characteristic diffraction peak at 2θ ≈ 27.8°**,** corresponding to the (002) plane, which is attributed to the interlayer stacking of conjugated aromatic layers and confirms the successful formation of graphitic carbon nitride (JCPDS No. 01-087-1526) [31]. The XRD pattern of pristine SrS (**Figure 5.4(b)**) shows well-defined diffraction peaks indexed to the (002), (112), (202), (220), (114), (213), (204), and (400) planes, confirming the crystalline phase of SrS in agreement with JCPDS No. 01-073-1180. The sharp diffraction peaks indicate the high crystallinity of the hydrothermally synthesized SrS nanoparticles [32].

For the 0.3% SrS/g-C_3N_4 NC (**Figure 5.4(c)**), diffraction peaks corresponding to both SrS and g-C_3N_4 are clearly observed without the appearance of any additional impurity peaks, confirming the successful formation of the heterostructured nanocomposite. The preservation of the characteristic (002) peak of g-C_3N_4 together with the prominent SrS reflections suggests that the composite formation does not alter the crystal structure of either constituent. The stacked XRD patterns (**Figure 5.4(d)**), further verify the

ISBN: 978-81-998984-9-3

Book DOI: 10.21467/books.186

coexistence of both phases and demonstrate that the hydrothermal process resulted in a highly crystalline and phase-pure SrS/g-C_3N_4 NC.

3.4. Ultraviolet Visible (UV-Vis.) absorption Spectroscopy

The optical absorption properties of pristine g-C_3N_4, SrS, and SrS/ g-C_3N_4 NC were investigated using UV–Visible spectroscopy, as shown in **Figure 5.5**. The absorption spectrum of pristine g-C_3N_4 (**Figure 5.5(a)**) exhibits strong absorption in the visible region with an absorption edge around 430 nm, which is characteristic of graphitic carbon nitride and confirms its visible-light response [31]. In contrast, pristine SrS shows a sharp absorption edge in the UV region owing to its wide band gap. Upon incorporation of g-C_3N_4 the SrS/ g-C_3N_4 NCs display enhanced absorption intensity and an extended absorption edge toward the visible region (**Figure 5.5(b)**), indicating improved light-harvesting capability due to the synergistic interaction between SrS and g-C_3N_4.

The optical band gap of the synthesized samples was estimated using the Tauc relation given in equation **(5.1)** versus photon energy (as depicted in **Figure 5.5c**).

$$\mathbf{A(}h\upsilon\mathbf{-}E_g\mathbf{)=(}\alpha h\upsilon\mathbf{)^2} \qquad \mathbf{(5.1)}$$

A stand for the material-related constant, $h\upsilon$ stands for the photon energy, is the adsorption coefficient, and moreover, for materials with a direct band gap, n is either 1/2 or 2, depending on the type of material. According to Tauc equation the calculated band gap of fabricated materials (g-C_3N_4, 0.1% SrS-gC_3N_4, 0.2% SrS-gC_3N_4, 0.3% SrS-gC_3N_4 are given in **Table 5.1.**

Table 5.1: Calculated band gaps of the prepared samples.

Samples	Band gap
g-C_3N_4	2.8 eV
0.1% SrS/ g-C_3N_4 NC	3.46 eV
0.2% SrS/ g-C_3N_4 NC	3.42 eV
0.3% SrS/ g-C_3N_4 NC	3.38 eV
SrS	3.50 eV

The calculated band gap energies were 2.89 eV for g-C_3N_4 and 3.50 eV for pristine SrS, while the SrS/ g-C_3N_4 NC exhibited gradually reduced band gap value to 3.38 eV for 0.3 wt.% g-C_3N_4, respectively. The progressive reduction in band gap with increasing g-C_3N_4 content can be attributed to the formation of a heterojunction and enhanced electronic interaction between SrS and g-C_3N_4, which facilitates charge transfer and broadens visible-light absorption. Such improved optical characteristics are expected to enhance electron transport and electrochemical activity, making the optimized **0**.3 wt.% SrS/ g-C_3N_4 NC a promising electrode material for energy storage applications.

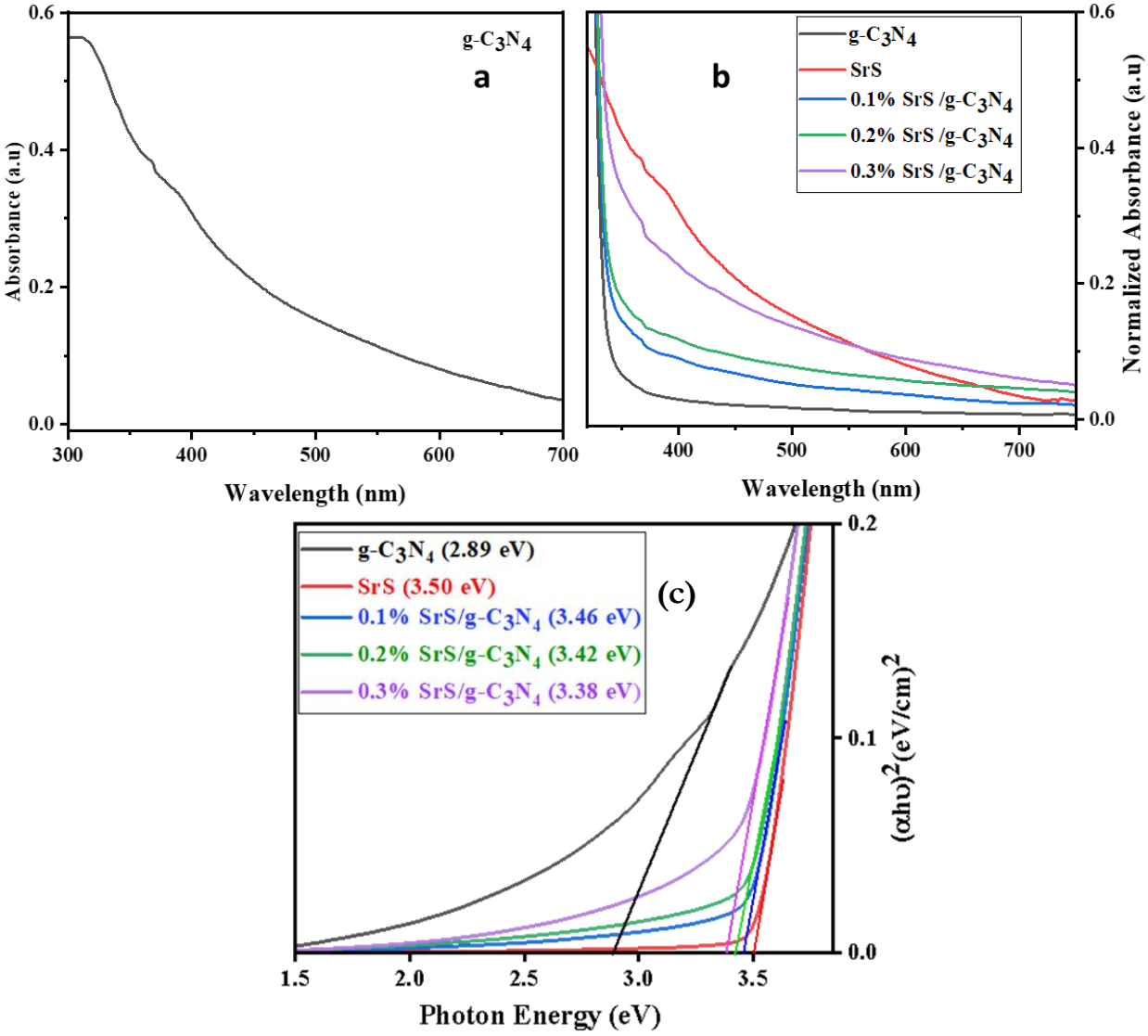

Figure 5.5 UV-Visible absorption spectra of **a)** SrS **b)** g-C_3N_4 and (0.1, 0.2 and 0.3)% SrS/g-C_3N_4 absorption spectra and Energy band gap of **c)** SrS, g-C_3N_4 and (0.1,0.2 and 0.3)% SrS/g-C_3N_4 NCs.

3.5. Raman Spectroscopy

Raman spectroscopy is a scientific technique that examines structural features by collecting data on crystal rotational and molecular vibrational effects. The spectra depicted in **Figure 5.6** are the results of synthesized material. Raman spectroscopy was also used to better understand how g-C_3N_4 and SrS interact. The clear D and G bands at 1350 cm^{-1} and 1640 cm^{-1} in the pure g-C_3N_4 catalyst demonstrate that interlayer stacking of aromatic systems, as in g-C_3N_4, occurs [10]. There has been minimal published work on the application of Raman spectroscopy to SrS nanostructures. SrS shows fine peaks at 450.52 cm^{-1} and 615.21

ISBN: 978-81-998984-9-3

Book DOI: 10.21467/books.186

cm^{-1}. Here composite sample 0.3% SrS/g-C_3N_4 shows peaks of both samples, SrS and g-C_3N_4 has a small shift and a grater intensity than pure samples. Complete agreement with our findings is

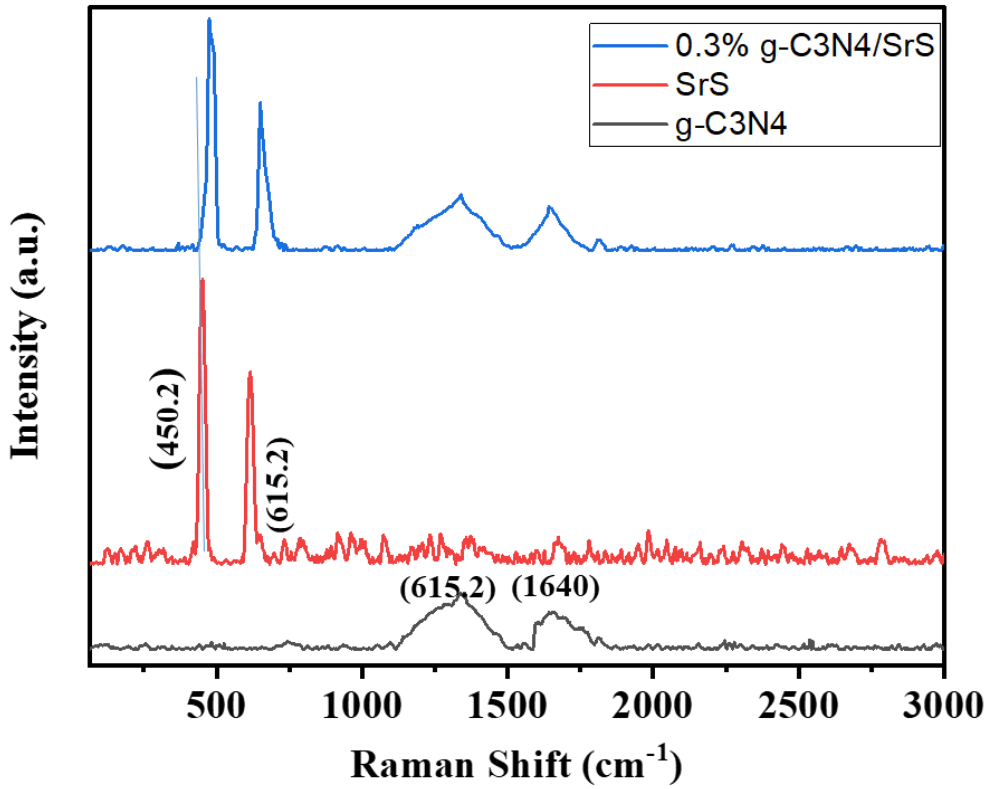

Figure 5.6 Raman spectroscopy of SrS, g-C_3N_4 and SrS/g-C_3N_4

shown by Raman scattering, which is thought to be particularly sensitive to the microstructures of nanocrystalline materials. Due to the material's excellent crystallinity, the SrS/g-C_3N_4 composite showed a higher intensity in Raman spectra.

3.6. Photoluminescence (PL) Spectroscopy

A useful tool for figuring out charge carrier transport, separation, and recombination is the Photoluminescence (PL) spectrum. The main area of photocatalytic activity is charge of photogenerated electron-hole pairs recombination rate. The hole and electron pair's recombination rate affects the PL intensity. Higher PL intensity results from quicker recombination rates, while lower recombination rates result in lower PL intensity. **Figure 5.7(a-c)** shows ambient temperature PL of g-C_3N_4.The emission peak was observed at 445nm excitation wavelength and was attributed to n-π^*electronic transitions. The energy of this peak was about comparable to the band gap energy of g-C_3N_4. It was discovered that the g-C3N4 sample had a greater PL intensity this indicates that the most optical recombination occurred in g-C3N4, which could reduce the photodegradation efficiency.

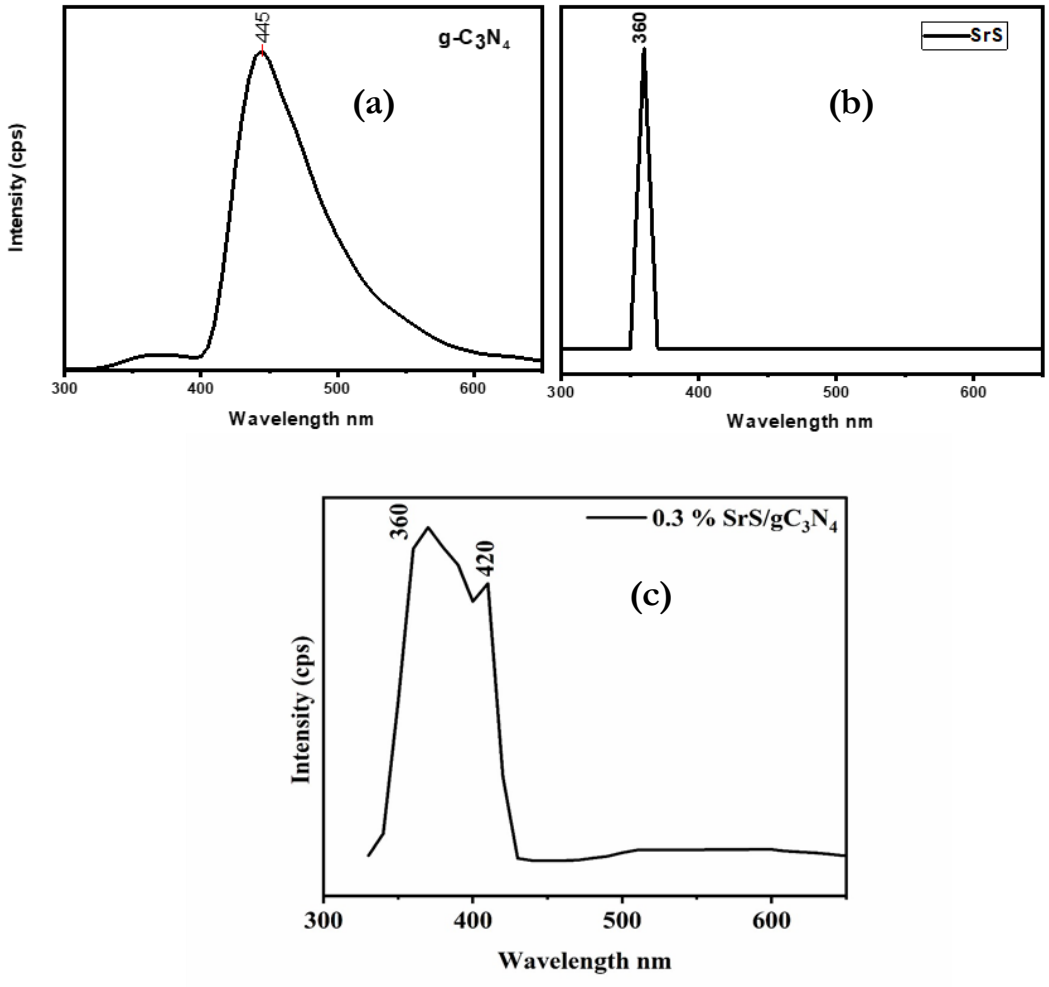

Figure 5.7 Room temperature PL spectra of a) SrS, b) g-C_3N_4, and c) SrS/g-C_3N_4.

SrS emission peak was observed at 360 nm, and pl spectra provide information about the energy levels of the material's electrons, the bandgap energy, and the kinds of transitions that take place as the electrons move between these levels. Nanocomposite (SrS/g-C_3N_4) showed two excitation band peaks at 360 nm and 410 nm which showed the g-C_3N_4 band decreases. PL spectra revealed the blue emission of the samples.

3.7. Electrochemical Investigation

3.7.1. Electrode Preparation

All the electrochemical behavior of the synthesized pure g-C_3N_4, SrS, 0.4% SrS/g-C_3N_4 was inspected by using an electrochemical instrument. The weights of 85% synthesized nano powder, 10% activated carbon, and 5% naflon were used to create the electrodes. As already indicated same weight was used by the author to create electrodes for g-C3N4, SrS, 0.4% SrS/g-C3N4 NSs. The slurry was first compressed onto nickel foam (1×1cm^2), and it was then dried for three hours at 60oC. About 3 mg of synthesized material was loaded on the fabricated electrode. A three-electrode configuration was adopted, with the electrolyte being

2M KOH and the counter electrode being platinum wire and Ag/AgCl, respectively.CV, GCD, and EIS were used to assess the effectiveness of the newly developed electrode.

3.7.2. Electrochemical Properties

The electrochemical performance of g-C_3N_4, SrS, and 0.3 wt.% SrS/g-C_3N_4 NC was evaluated by cyclic voltammetry (CV) in the potential window of −0.2 to 0.6 V at scan rates ranging from 5 to 100 mV s^{-1}, as shown in **Figure 5.8(a-c)**. All samples exhibit distinct anodic and cathodic redox peaks, indicating that the charge storage mechanism is predominantly governed by faradaic pseudocapacitive reactions [33]. As the scan rate increases, the current response increases proportionally while the overall CV profile is well maintained, demonstrating good electrochemical reversibility and rapid charge-transfer kinetics.

Among the investigated samples, the 0.3 wt.% SrS/g-C_3N_4 NC exhibits the largest enclosed CV area and the highest current response, indicating a superior charge storage capability compared to pristine SrS and g-C_3N_4. The enhanced electrochemical performance is attributed to the synergistic interaction between SrS and g-C_3N_4, which provides abundant electroactive sites, facilitates electron transport, and accelerates electrolyte ion diffusion. These results demonstrate that the formation of the SrS/g-C_3N_4 NC effectively enhances the pseudocapacitive behavior, making it a promising electrode material for high-performance SC applications. The C_p values of all electrodes shown in **Figure 5.8(d**).

Peak current increases as the scan rate increases, showing that interfacial faradic redox reaction kinetics and ionic electronic transport rates are fast enough at the current scan rate. **Equation 5.2** was utilized to calculate the specific capacitance of synthesized electrodes [34].

$$C_p = \frac{A}{2KmV} \qquad (5.2)$$

Here m is active material's mass. The scan rate is K. Potential window is ΔV (V_2-V_1) and the absolute area is A. It is evident that 0.3% offers the highest C_p value as displayed in **Table 5.2**.

Table 5.2 Specific capacitance of the synthesized material at different scan rates.

Electrode Material	**100mVs^{-1}**	**75mVs^{-1}**	**50mVs^{-1}**	**25mVs^{-1}**	**15mVs^{-1}**	**10mVs^{-1}**	**5mVs^{-1}**
SrS	74	99	134	185	239	269	317
g-C_3N_4	62	67	113	155	201	227	267
0.3% SrS/g-C_3N_4	98	125	161	294	401	484	605

The charge storage performance of SrS, g-C_3N_4, and 0.3 wt.% SrS/g-C_3N_4 electrodes was investigated by galvanostatic charge–discharge (GCD) measurements at current densities of 2, 2.5, and 3 A g^{-1}, as shown in **Figure 5.9(a–c)**. All electrodes exhibit nearly symmetric charge–discharge profiles with distinct voltage plateaus, confirming the pseudocapacitive charge storage behavior and good electrochemical reversibility [35]. Among the investigated samples, the 0.3 wt.% SrS/g-C_3N_4 NC displays the longest discharge time,

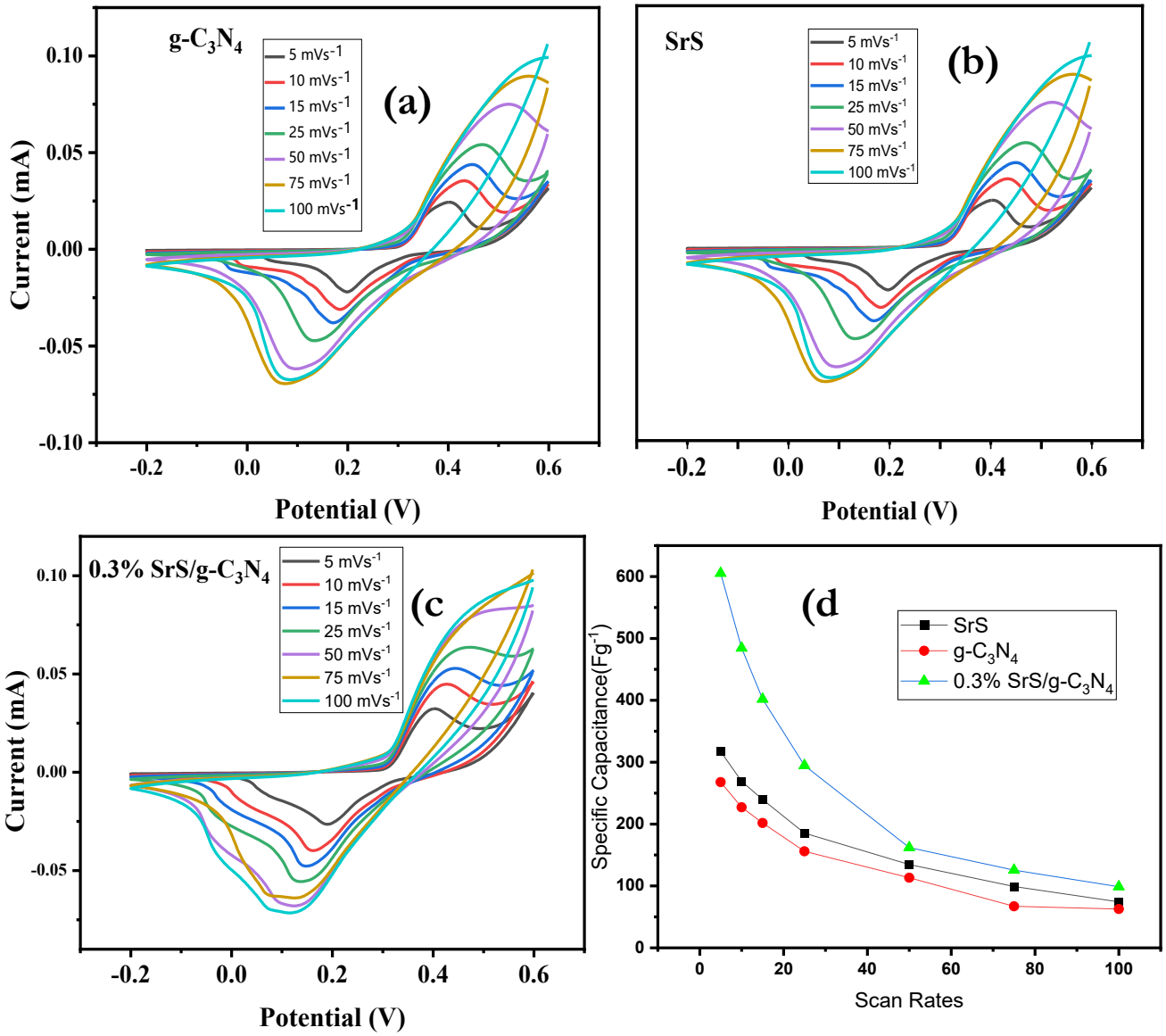

Figure 5.8. Cyclic voltammetry of a) SrS, b) pure g-C_3N_4, c) 0.4% SrS/g-C_3N_4 and d) C_p values of all samples.

indicating the highest specific capacitance. The enhanced electrochemical performance is attributed to the synergistic interaction between SrS and g-C_3N_4 which facilitates rapid electron transport, provides abundant electroactive sites, and improves electrolyte ion diffusion [1]. Based on the GCD discharge time result, equation **5.3** was used to calculate the particular C_p value of fabricated electrodes and summarize in **Table 5.3.**

$$C_p = \frac{I \times \Delta t}{m \times \Delta V} \qquad (5.3)$$

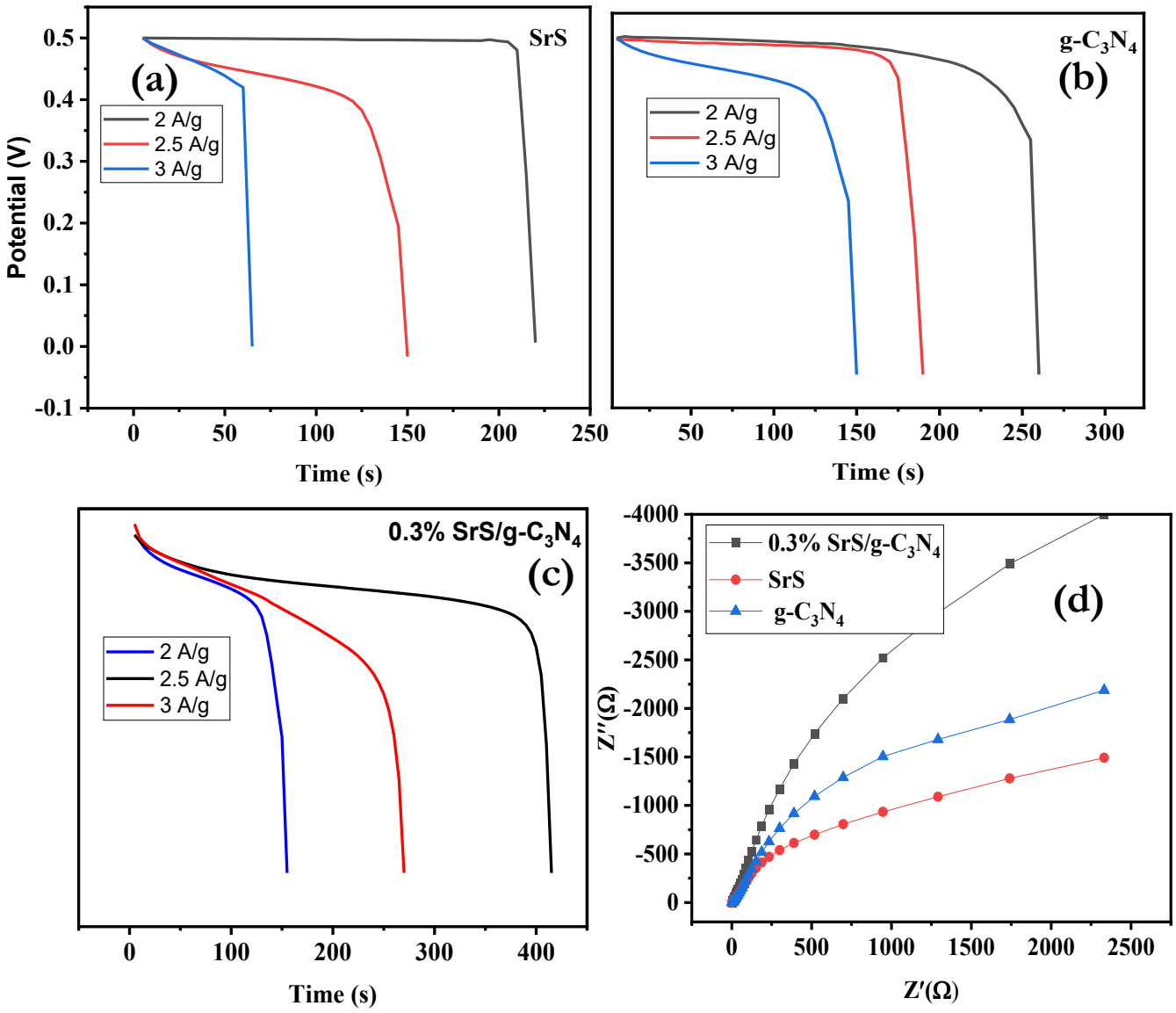

Figure 5.9. Galvanostatic charge-discharge of a) SrS, b) g-C_3N_4, c) 0.4% SrS/g-C_3N_4, and d) EIS curve of SrS, g-C_3N_4, 0.4% SrS/g-C_3N_4. e) Scan rate vs specific capacitance of (SrS, g-C_3N_4, 0.3% SrS/g-C_3N_4)

Where I is discharging current, m shows the active mass Δt shows discharge time, and ΔV represent discharge potential window. Due to reduction in voltage drop and a lack of active material for the redox reaction, specific capacitance steadily decreased as current density rises. Maximum C_p value from the GCD curve at 2 Ag^{-1} was calculated to be 820 Fg^{-1}, which is equivalent to C_p value obtained from cv (605F/g).

3.7.3. Electrochemical Impedance Spectroscopy

The electrochemical impedance spectra (Nyquist plots) of the synthesized electrodes are presented in **Figure 5.9(d)**. All samples exhibit a small semicircle in the high-frequency region followed by an inclined line in the low-frequency region, representing the charge-transfer resistance and ion diffusion behavior, respectively. The 0.3 wt.% SrS/g-C_3N_4 NC exhibits the smallest semicircle and the steepest low-frequency

slope, indicating lower charge-transfer resistance and enhanced ionic conductivity compared with pristine SrS and g-C_3N_4. These results demonstrate that the heterostructure effectively promotes interfacial electron transport and accelerates electrochemical reaction kinetics, leading to improved energy storage performance [35]. The diameter semicircle of the 0.4% SrS/g-C_3N_4 sample is significantly smaller in comparison to the SrS and pure g-C_3N_4 samples. The smaller the semicircle has a low change transfer resistance and a high conductivity. The vertical line which also shows that electrodes are nearing an idea capacitor, caused by ionic diffusion between electrode surface and electrolyte.

Table 5.3 Specific capacitance, energy and power density of synthesized material at various current densities.

Electrode Material	Discharge Time (s)	Current Density (A/g)	Specific Capacitance (F/g)	Energy Density (Wh/Kg)	Power Density (W/Kg)
SrS	225	1	450	15.625	250
	145	1.5	435	15.104	375
	60	2	240	8.333	500
g-C_3N_4	295	1	590	20.486	250
	185	1.5	555	19.270	375
	145	2	480	16.66	500
SrS-0.3% g-C_3N_4	410	1	820	28.472	250
	265	1.5	795	27.604	375
	150	2	600	20.833	500

4. Conclusion

In this study, SrS/g-C_3N_4 NCs were successfully synthesized for the first time using a simple and cost-effective hydrothermal method. The prepared nanocomposites exhibited enhanced structural, optical, and electrochemical properties, demonstrating the synergistic interaction between SrS and g-C_3N_4XRD analysis confirmed the successful formation of the nanocomposite with improved crystallinity, while SEM revealed the integration of rod-like SrS with sheet-like g-C_3N_4. The elemental composition and successful incorporation of g- C_3N_4 were further verified by EDX and Raman spectroscopy. UV–Vis analysis showed a significant reduction in the direct band gap, accompanied by a red shift in the absorption edge, indicating enhanced visible-light absorption. Photoluminescence measurements exhibited blue emission centered at 445 nm and suggested suppressed electron–hole recombination, favoring efficient charge separation. Electrochemical studies demonstrated superior charge storage behavior and lower charge-transfer resistance for the composite compared with pristine SrS. The optimized SrS/g- C_3N_4 NC delivered a high

ISBN: 978-81-998984-9-3

Book DOI: 10.21467/books.186

specific C_p value of of 850 F g^{-1} at a current density of 0.5 A g^{-1}, highlighting its excellent electrochemical performance. Overall, the facile synthesis strategy and the improved optical and electrochemical characteristics demonstrate that SrS/g C_3N_4 NCs are promising candidates for energy srorage and other optoelectronic applications. These findings provide an effective strategy for designing high-performance semiconductor heterostructures for sustainable energy conversion and storage technologies.

5. Publisher's Note

AIJR remains neutral with regard to jurisdictional claims in published maps and institutional affiliations.

Author's Detail

Muhammad Arshad Kamran*, Wajeeha Sameen, Areej Rani
Department of Physics, University of Okara, Okara, Pakistan.

*Corresponding author

How to Cite this Chapter:

M. A. Kamran, W. Sameen, A. Rani, "Facile Synthesis and Characterization of Strontium Sulfide Incorporated Graphitic Carbon Nitride Nanocomposite for Energy Storage Applications," in *Emerging Functional Materials for a Sustainable Energy Future*, M. A. Kamran, Ed. India: AIJR Publisher, 2026, pp. 75-92. ISBN: 978-81-998984-9-3, doi: 10.21467/books.186.5

References

[1] M. A. Kamran, W. Ali, and T. Alharbi, "Facile synthesis of novel cobalt molybdenum sulfide-graphitic carbon nitride (CoMoS4/g-C3N4) nanocomposite electrode for improved supercapacitor and photocatalytic applications," *Journal of Energy Storage,* vol. 100, p. 113722, 2024.

[2] A. Kashaf, M. A. Kamran, S. Ullah, A. Rani, T. Alharbi, and A. Razzaq, "Bifunctional vanadium-doped barium molybdate nanostructures for high-performance supercapacitors and efficient photocatalytic degradation," *Physica B: Condensed Matter,* p. 418214, 2025.

[3] S. Ullah, M. A. Kamran, and T. Alharbi, "Strontium cobalt oxide/graphitic carbon nitride hybrid nanostructures: A green-engineered platform for sustainable energy storage," *Journal of Energy Storage,* vol. 163, p. 122201, 2026.

[4] A. Ali *et al.*, "Investigation of ZnO@ CdS nanocomposite with amplified photocatalytic H2 production under visible light irradiation," *Surfaces and Interfaces,* vol. 52, p. 104836, 2024.

[5] Y. Li, M. Zhou, B. Cheng, and Y. Shao, "Recent advances in g-C3N4-based heterojunction photocatalysts," *Journal of Materials Science & Technology,* vol. 56, pp. 1-17, 2020.

[6] S. Komarneni, "Nanocomposites," *Journal of Materials Chemistry,* vol. 2, no. 12, pp. 1219-1230, 1992.

[7] D. S. Su *et al.*, "Metal-free heterogeneous catalysis for sustainable chemistry," *ChemSusChem: Chemistry & Sustainability Energy & Materials,* vol. 3, no. 2, pp. 169-180, 2010.

[8] Y. Wang, X. Wang, and M. Antonietti, "Polymeric graphitic carbon nitride as a heterogeneous organocatalyst: from photochemistry to multipurpose catalysis to sustainable chemistry," *Angewandte Chemie International Edition,* vol. 51, no. 1, pp. 68-89, 2012.

[9] S. Chu *et al.*, "Band structure engineering of carbon nitride: in search of a polymer photocatalyst with high photooxidation property," *Acs Catalysis,* vol. 3, no. 5, pp. 912-919, 2013.

[10] G. Dong, Y. Zhang, Q. Pan, and J. Qiu, "A fantastic graphitic carbon nitride (g-C3N4) material: electronic structure, photocatalytic and photoelectronic properties," *Journal of Photochemistry and Photobiology C: Photochemistry Reviews,* vol. 20, pp. 33-50, 2014.

[11] Y. Zhang, T. Mori, J. Ye, and M. Antonietti, "Phosphorus-doped carbon nitride solid: enhanced electrical conductivity and photocurrent generation," *Journal of the American Chemical Society,* vol. 132, no. 18, pp. 6294-6295, 2010.

[12] X. Wang, S. Blechert, and M. Antonietti, "Polymeric graphitic carbon nitride for heterogeneous photocatalysis," *Acs Catalysis,* vol. 2, no. 8, pp. 1596-1606, 2012.

[13] D. R. Paul, S. Gautam, P. Panchal, S. P. Nehra, P. Choudhary, and A. Sharma, "ZnO-modified g-C3N4: a potential photocatalyst for environmental application," *ACS omega,* vol. 5, no. 8, pp. 3828-3838, 2020.

[14] Y. Zhu, Y. Xu, Y. Hou, Z. Ding, and X. Wang, "Cobalt sulfide modified graphitic carbon nitride semiconductor for solar hydrogen production," *International journal of hydrogen energy,* vol. 39, no. 23, pp. 11873-11879, 2014.

[15] R. C. Pawar, V. Khare, and C. S. Lee, "Hybrid photocatalysts using graphitic carbon nitride/cadmium sulfide/reduced graphene oxide (g-C3N4/CdS/RGO) for superior photodegradation of organic pollutants under UV and visible light," *Dalton Transactions,* vol. 43, no. 33, pp. 12514-12527, 2014.

[16] F. Jiang, T. Yan, H. Chen, A. Sun, C. Xu, and X. Wang, "A g-C3N4–CdS composite catalyst with high visible-light-driven catalytic activity and photostability for methylene blue degradation," *Applied Surface Science,* vol. 295, pp. 164-172, 2014.

[17] Z. Li, L. Wu, L. Wang, A. Gu, and Q. Zhou, "Nickel cobalt sulfide nanosheets uniformly anchored on porous graphitic carbon nitride for supercapacitors with high cycling performance," *Electrochimica Acta,* vol. 231, pp. 617-625, 2017.

[18] P. Macheroux, "UV-visible spectroscopy as a tool to study flavoproteins," in *Flavoprotein protocols*: Springer, 1999, pp. 1-7.

[19] J. Wu *et al.*, "The genome of pear (Pyrus bretschneideri Rehd.)," *Genome research,* p. gr. 144311.112, 2012.

[20] J.-X. Sun *et al.*, "Fabrication of composite photocatalyst g-C3N4–ZnO and enhancement of photocatalytic activity under visible light," *Dalton Transactions,* vol. 41, no. 22, pp. 6756-6763, 2012.

[21] L. Huang *et al.*, "Visible-light-induced WO3/g-C3N4 composites with enhanced photocatalytic activity," *Dalton Transactions,* vol. 42, no. 24, pp. 8606-8616, 2013.

[22] S. Vignesh *et al.*, "Fabrication of Ag/Ag2O incorporated graphitic carbon nitride based ZnO nanocomposite for enhanced Z-scheme photocatalytic performance of various organic pollutants and bacterial disinfection," *Journal of Environmental Chemical Engineering,* vol. 9, no. 5, p. 105996, 2021.

[23] S. Vinoth, R. Ramaraj, and A. Pandikumar, "Facile synthesis of calcium stannate incorporated graphitic carbon nitride nanohybrid materials: A sensitive electrochemical sensor for determining dopamine," *Materials Chemistry and Physics,* vol. 245, p. 122743, 2020.

[24] T. Liu *et al.*, "Integrative hinge based on shape memory polymer composites: Material, design, properties and application," *Composite Structures,* vol. 206, pp. 164-176, 2018.

[25] J. Wang, P. Guo, Q. Guo, P. G. Jönsson, and Z. Zhao, "Fabrication of novel g-C3N4/nanocage ZnS composites with enhanced photocatalytic activities under visible light irradiation," *CrystEngComm,* vol. 16, no. 21, pp. 4485-4492, 2014.

[26] D. Muthu, S. Vargheese, Y. Haldorai, and R. T. R. Kumar, "NiMoO4/reduced graphene oxide composite as an electrode material for hybrid supercapacitor," *Materials Science in Semiconductor Processing,* vol. 135, p. 106078, 2021.

[27] R. R. Devi, S. Thanikaikarasan, and S. Ramanathan, "Hydrothermal synthesis of g-C3N4/NiMoO4 nanorod composites for high-performance symmetric supercapacitors," *Journal of Energy Storage,* vol. 177, p. 123485, 2026.

[28] R. Liang *et al.*, "High performance g-C3N4@ NiMoO4/CoMoO4 electrode for supercapacitors," *Journal of Solid State Chemistry,* vol. 307, p. 122845, 2022.

[29] M. Saadati pour, M. Delyanee, and M. Z. Pedram, "Innovative synthesis and advancement strategies for GCN as supercapacitor electrodes: A comprehensive review revealing new insights," *ACS Applied Energy Materials,* vol. 8, no. 7, pp. 3997-4031, 2025.

[30] J. Nallapureddy *et al.*, "Synergistic dual-active-site coupling of carbon nitride and nickel molybdate nanorods for multifunctional energy systems," *Journal of Power Sources,* vol. 666, p. 239193, 2026.

[31] W.-J. Ong, L.-L. Tan, Y. H. Ng, S.-T. Yong, and S.-P. Chai, "Graphitic carbon nitride (g-C3N4)-based photocatalysts for artificial photosynthesis and environmental remediation: are we a step closer to achieving sustainability?," *Chemical reviews,* vol. 116, no. 12, pp. 7159-7329, 2016.

[32] R. Tholkappiyan, R. Satheesh Kumar, L. Mohamed Azarudeen, G. Anand Kumar, K. Vishista, and F. Hamed, "Facile synthesis of Cr-doped SrS phosphor: an investigations on structural, vibrational, morphological and photoluminescence properties," *Materials Focus,* vol. 5, no. 4, pp. 342-346, 2016.

[33] P. Simon and Y. Gogotsi, "Materials for electrochemical capacitors," *Nature materials,* vol. 7, no. 11, pp. 845-854, 2008.

[34] R. Lin *et al.*, "A general method for boosting the supercapacitor performance of graphitic carbon nitride/graphene hybrids," *Journal of Materials Chemistry A,* vol. 5, no. 48, pp. 25545-25554, 2017.

[35] P. Yadav, E. J. J. o. A. Sinha, and Compounds, "Structural, photophysical and microwave dielectric properties of α-ZnMoO4 phosphor," vol. 795, pp. 446-452, 2019.